

Revisiting the Ridgecrest aftershock catalog using a modified source-scanning algorithm applied to multiple dense local arrays

Eyal Shimony; Asaf Inbal; Ariel Lellouch
Tel Aviv University

Abstract

We develop and implement a modified Source-Scanning Algorithm (SSA) method to estimate absolute event locations in the presence of velocity model errors. We split the recording array into sub-arrays of clustered receivers, for which relative travel-times errors are limited. We apply a conventional SSA using both P- and S-waves to each sub-array and combine the estimations using a probabilistic scheme. We apply the method to 688 aftershocks recorded by 197 short-period geophones deployed in 2019 as part of the Ridgecrest dense array. We compare 339 locations to a relocated catalog built using the same 1-D velocity model of the area. We qualitatively compare location estimations using the alignment of time-shifted seismograms. Our locations yield, in most cases, better alignment, and are 2 km deeper on average. For events in the northern part of the study area, our locations are shifted to the northeast.

Introduction/Background

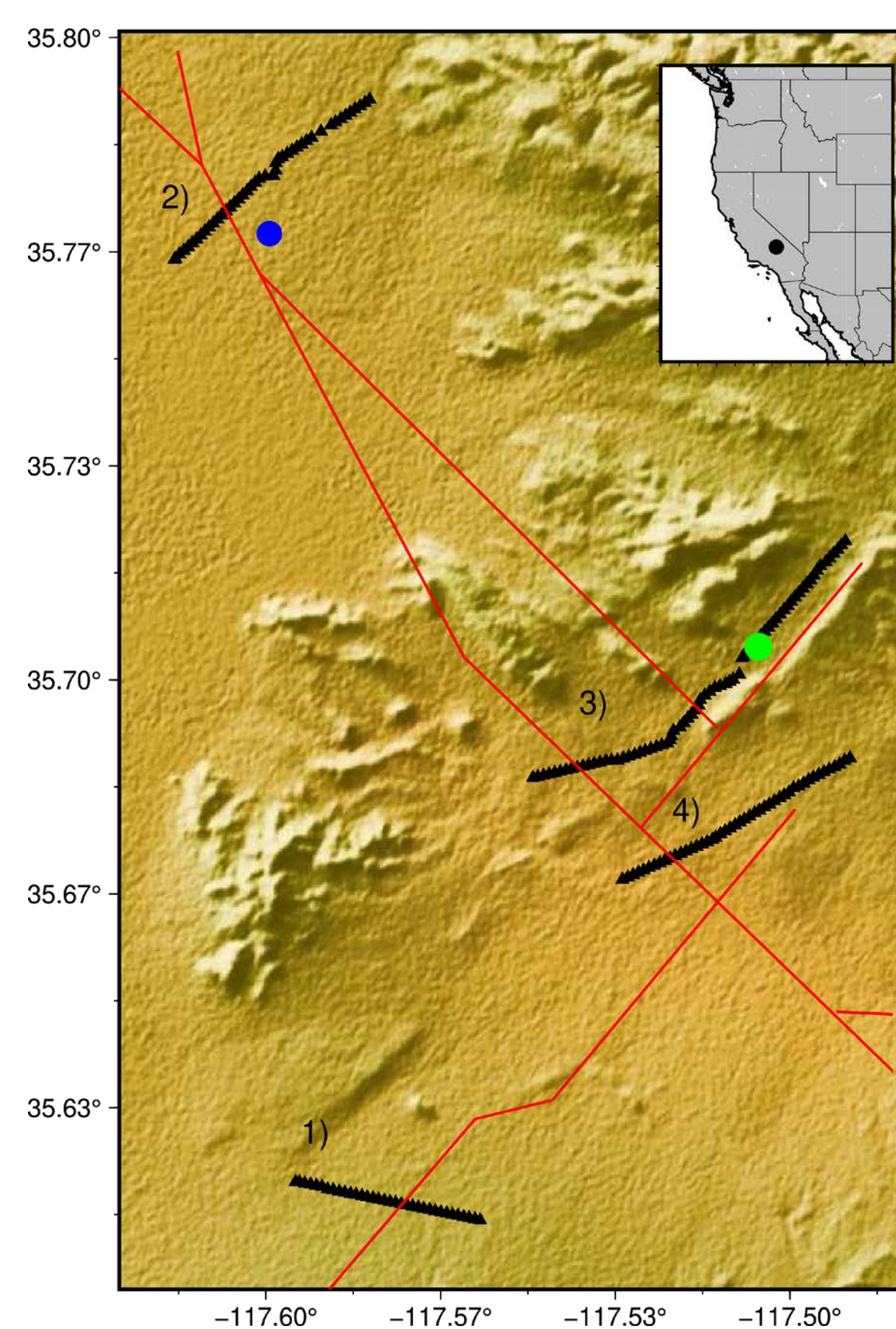


Figure 1: Topographic map of the Ridgecrest area. Location of faults, as interpreted at depth by Ross et al. (2019), are indicated by red curves. The seismic stations are indicated by black triangles. Dense station lines, numbered from 1 to 4 (100 m nominal distance between stations) intersect with the faults. The M_w 7.1 event and the M_w 6.4 event epicenters are in blue and green, respectively.

Data and Methodology

Our method relies on the idea that the relative propagation time errors between the source-station pairs (s, r_1) , (s, r_2) become smaller as the distance between the stations (r) reduces. Therefore, we separately apply an SSA-type algorithm on each cluster of stations, and then impose maximal agreement between the individual results.

$$br(\eta) = \frac{1}{2L} \sum_{l=1}^L s_l^P(t_l^P) + B \cdot s_l^S(t_l^S) - A \cdot \text{MAD}(\{t_l^P, t_l^S | 1 \leq l \leq L\})$$

$$s_l^{P|S}(t) = \frac{1}{N_l} \sum_{n=1}^{N_l} \frac{1}{2M+1} \sum_{m=-M}^M \left(\text{AGC}_{(P|S)}(v_{n,l}(t - \tau_{\eta n l}^{P|S} + m \cdot dt)) \right)^2$$

l – sub-array index; L – number of sub-arrays; n – intra-sub-array station index; N_l – number of stations in the l^{th} sub-array; $[-M, M]$ is the smoothing window; $\tau_{\eta n l}^{P|S}$ – P- or S-wave travel time from location η to station n, l ; dt – sampling rate; $v_{n,l}$ – the recorded velocity at station n, l ; $t_l^{P|S}$ – the estimated origin time using the P- or S-wave alignment on sub-array l .

$$Pnn(\eta) = \left(1 + \exp \left(- \frac{br(\eta) - \max_{\eta} br(\eta)}{\max_{\eta} br(\eta) / (20 \ln(2e - 1))} \right) \right)^{-1}$$

$$P(\eta) = \frac{Pnn(\eta)}{\sum_{\eta} Pnn(\eta)}$$

$$\eta = \underset{y \in V}{\text{argmin}} \sum_l P(\eta_l) \|\eta_l - y\|$$

V is the region of interest

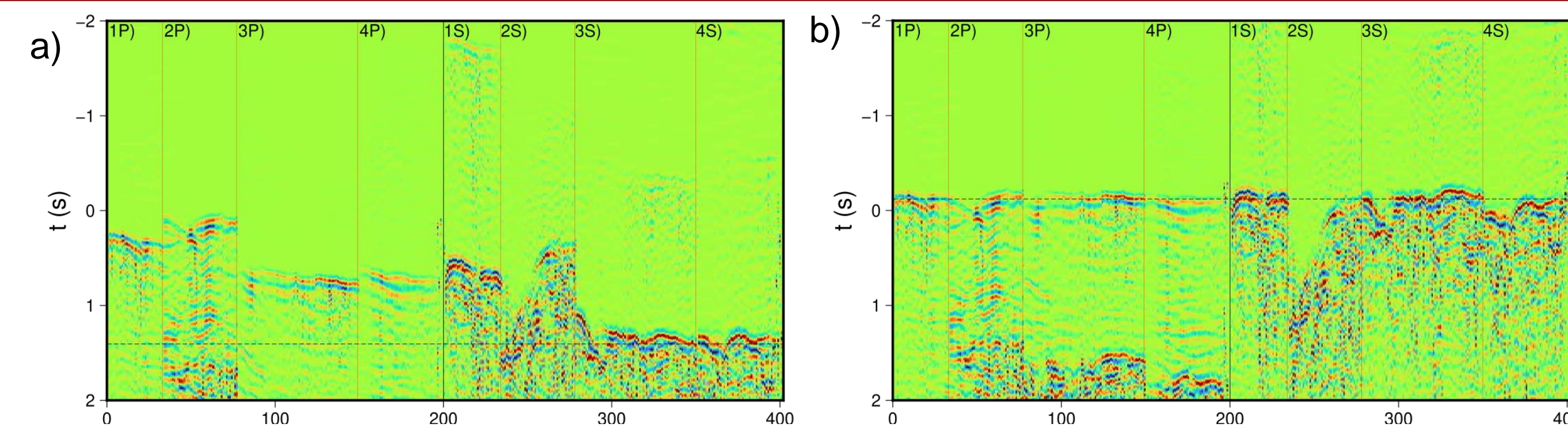


Figure 2: Time shifted seismograms of field records constructed at two locations estimated using (a) conventional SSA brightness and (b) our modified brightness. In (a), the phases are misaligned, indicating a wrong location.

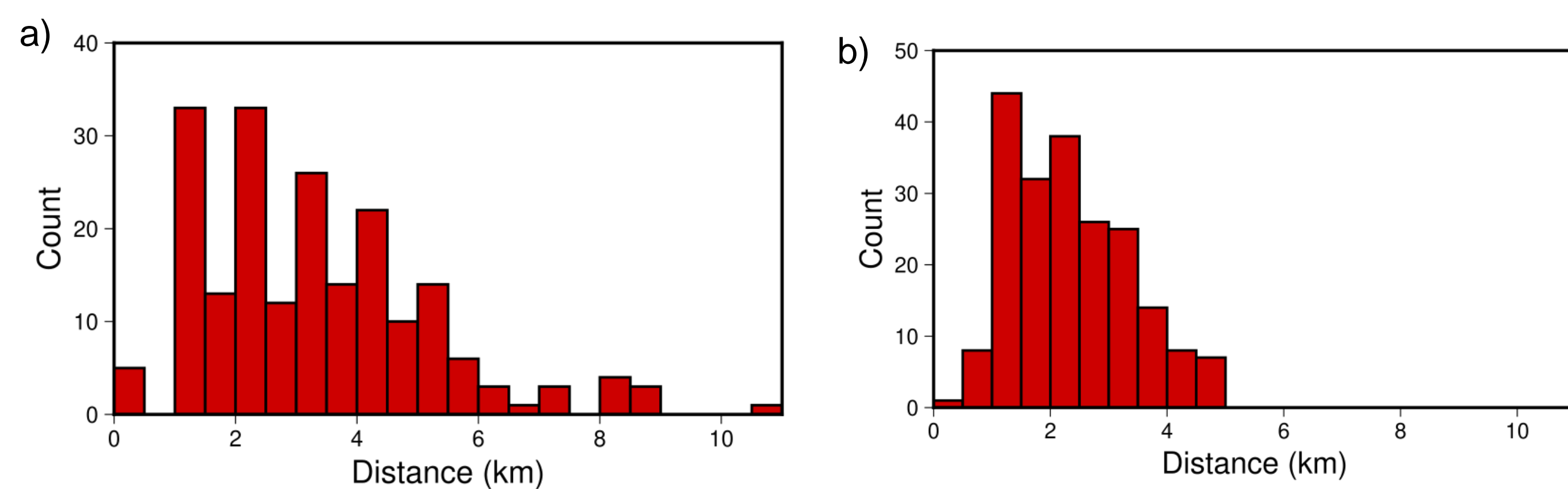


Figure 3: Histograms of the distance between the true locations and those estimated by (a) The SSA method (b) The modified SSA method in a synthetic test including significant velocity errors. The average errors are 2.34 and 3.3 km, respectively. The modified SSA method errors are all below 5 km, whereas the SSA method errors are as high as 11 km.

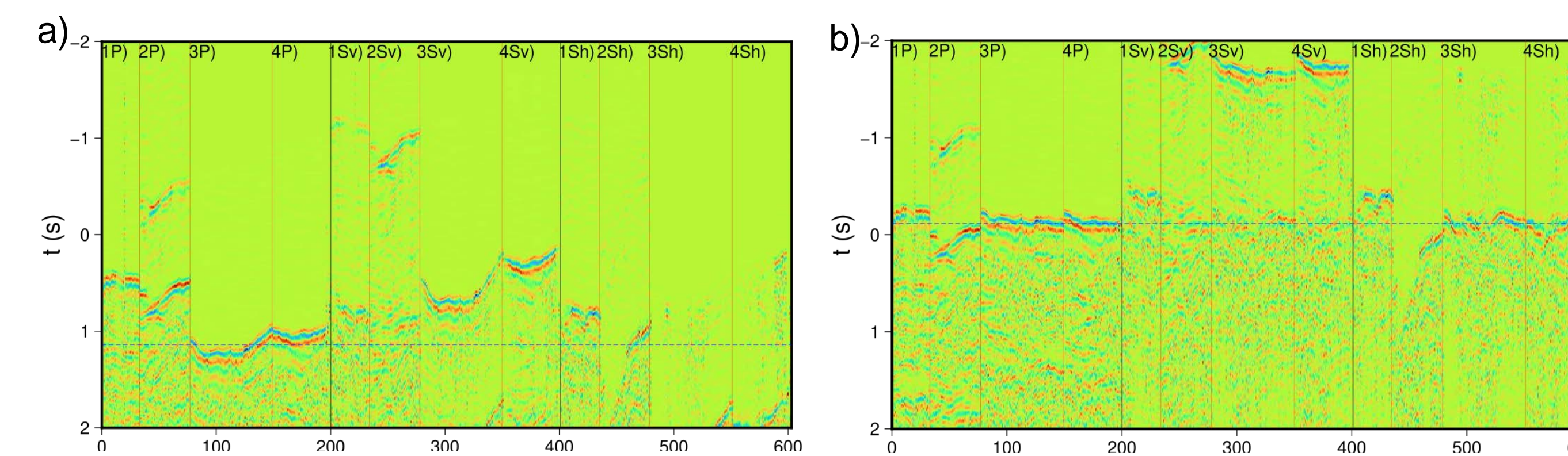


Figure 4: Comparison between time-shifted seismograms constructed at the cataloged location (a) and the location estimated in this study (b). Each array is separated into three main parts, delimited by vertical black lines. (1P-4P) – vertical seismograms shifted by the P-wave propagation times; (1Sv-4Sv) – vertical seismograms shifted by the S-wave propagation times; (1Sh-4Sh) – N-S seismograms shifted by the S-wave propagation times. The origin time estimated from the shifted seismograms is indicated by a horizontal dashed black line. The location in (a) is erroneous as the phases are severely misaligned.

Results

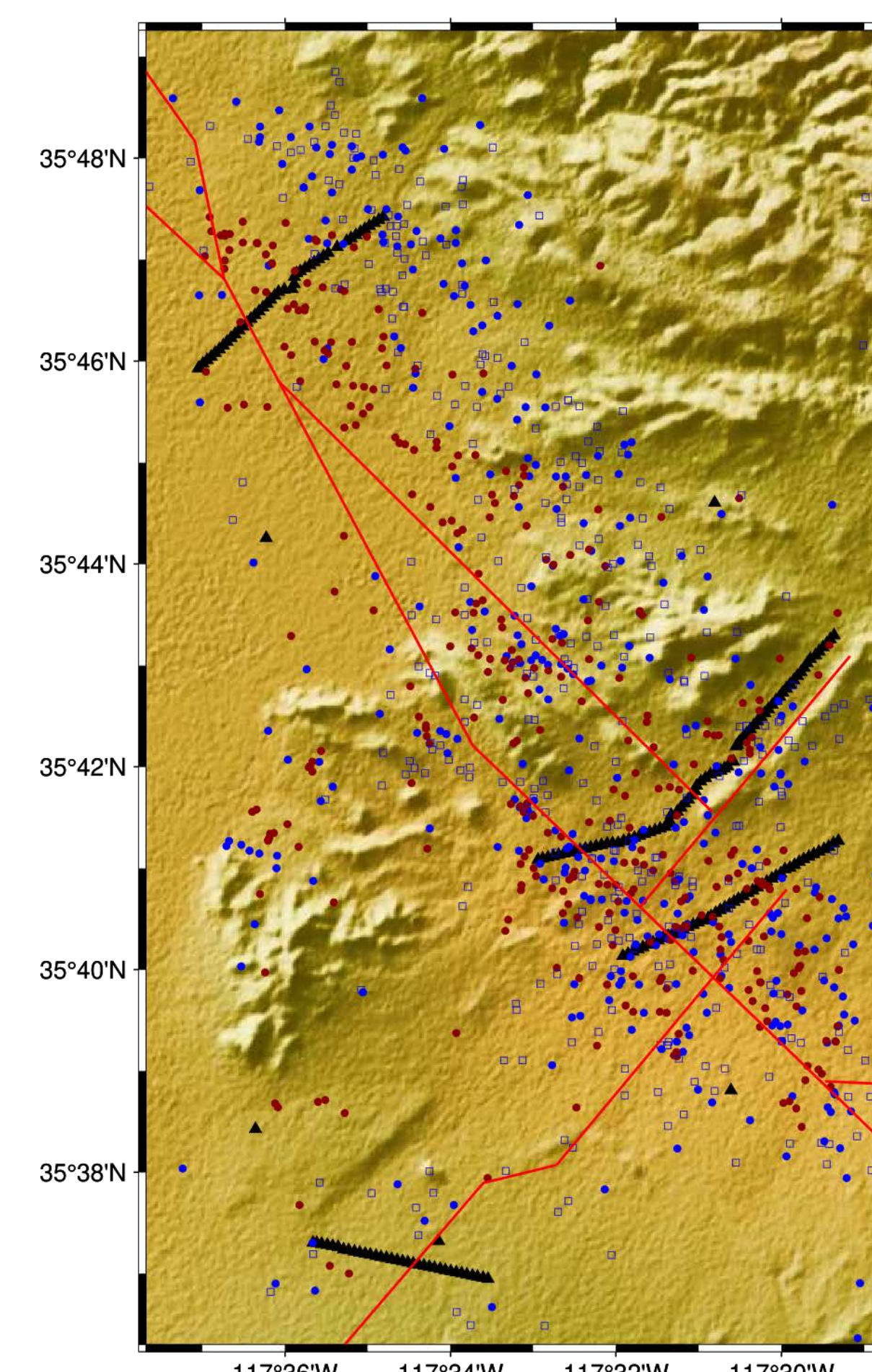


Figure 5: Estimated event locations for this study (blue discs), their comparison with Shelly (2020) (dark red discs), and this study's estimations of locations that occurred after July 17, 0:00 UTC (blue squares). Ross et al. (2019) interpretation of the fault geometry at depth (red lines) and station locations (black triangles) are the same as in Figure 1.

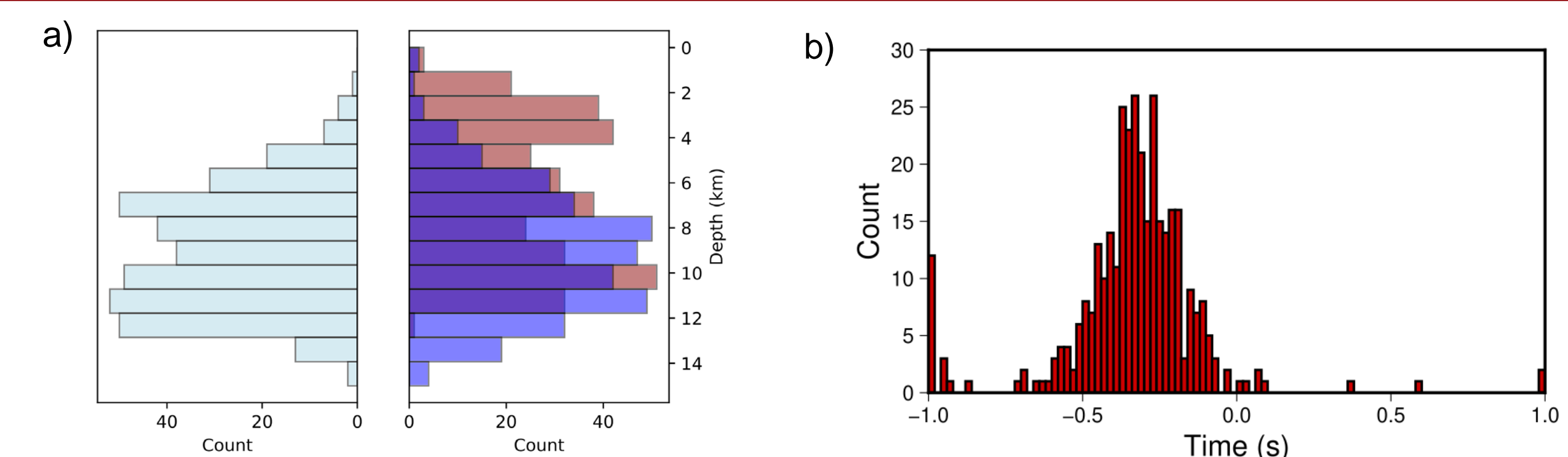


Figure 6: (a) Histogram of estimated events' depth: this study (blue) and cataloged locations (red) for the events that occurred until July 17, 0:00 UTC, and this study (cyan) for events that occurred later. (b) Histogram of the differences in origin times estimated in this study and the benchmark catalog for the events that occurred until July 17, 0:00 UTC. Locations in this study are consistently deeper, which leads to the origin times estimations being consistently earlier.

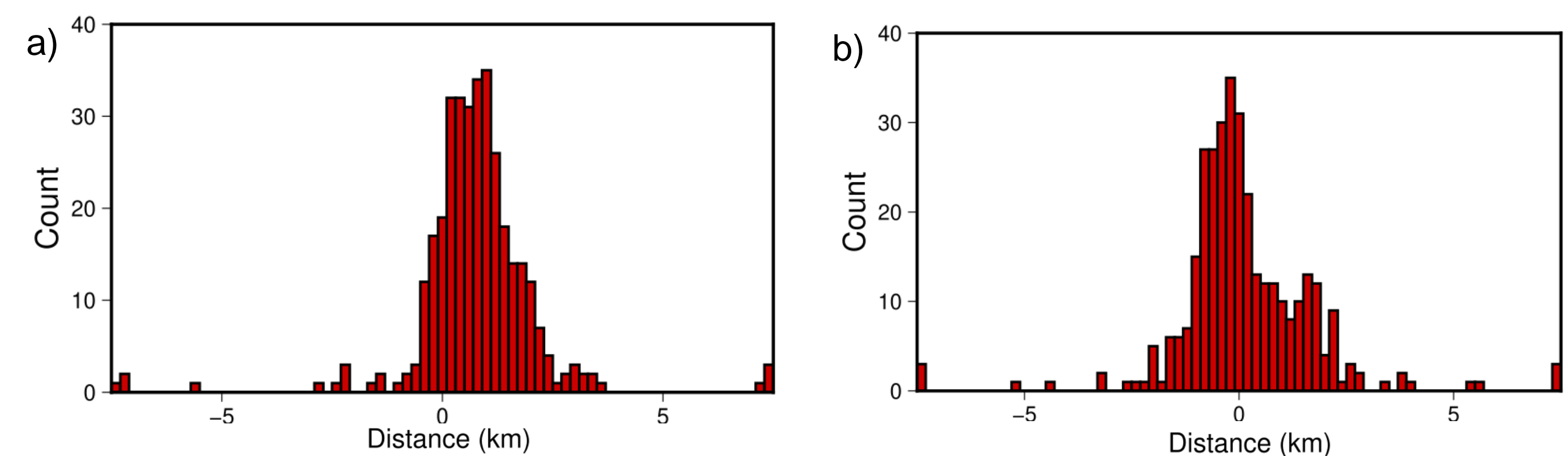


Figure 7: Histograms of the difference between event locations calculated by Shelly (2020) and this study. (a) East-West direction. (b) North-South direction. We observe a slight eastwards drift, related to the events in the northern part of the model. However, there is no noticeable bias in the north-south axis.

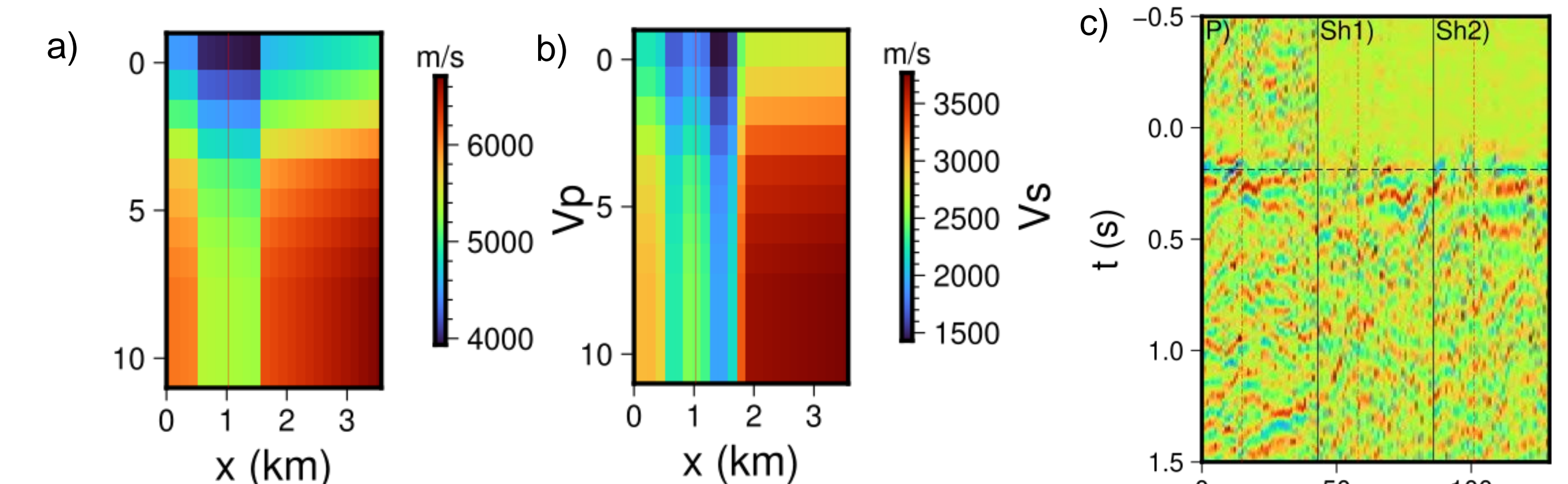


Figure 8: A toy example of using gather flattening as a tool for manual velocity inversion. Here, we tried to flatten the gather of the second line, which deviates from flatness in Figures 2 and 4 due to the complex velocity structure around it. (a,b) 2-D P- and S-wave velocity models, respectively, used to build the time-shifted seismograms in (c). (P) are the vertical seismograms shifted by the P-wave velocity, (Sh1) are the E-W seismograms shifted by the S-wave velocity, and (Sh2) are the N-S seismograms shifted by the S-wave velocity, separated by black vertical lines. The magnitude of change in velocity is very significant.

Summary/Conclusion

The local, high-resolution array deployed over the Ridgecrest region enables the absolute localization of individual earthquakes. We develop a modified SSA method that splits the array into sub-arrays of clustered receivers and utilizes both P- and S-phases. We apply it to four days of recorded aftershocks to estimate event locations and their uncertainty. We qualitatively evaluate location accuracy by inspecting the flatness of the time-shifted seismograms. According to this metric, our location method yields superior results to both conventional SSA, applied to the same data, and a relocated catalog built using a regional network. However, velocity-driven biases in our estimations probably remain. Our estimated locations are on average deeper than the cataloged ones, and the events in the northern part of the study area are shifted towards the north-east. This study shows that using dense arrays, for which relative travel-time errors are limited, may be used to overcome the effect of velocity model errors. Notwithstanding, it emphasizes the importance of high-quality velocity models for location using local arrays, especially near complex geological structures.

References

Z. E. Ross, B. Idini, Z. Jia, O. L. Stephenson, M. Zhong, X. Wang, Z. Zhan, M. Simons, E. J. Fielding, S.-H. Yun, E. Hauksson, A. W. Moore, Z. Liu, and J. Jung. Hierarchical interlocked orthogonal faulting in the 2019 ridgecrest earthquake sequence. *Science*, 366 (6463):346–351, 10 2019. doi: 10.1126/science.aaz0109.

R. Shelly. A high-resolution seismic catalog for the initial 2019 ridgecrest earthquake sequence: Foreshocks, aftershocks, and faulting complexity. *Seismological Research Letters*, 91(4):1971–1978, 1 2020. doi: 10.1785/0220190309.

Acknowledgements

This research was supported by the Israeli Science Foundation (ISF) under grant #2775/21